Development of numerical analysis and methane sensing application of highly sensitive quantum crystals based on tin dioxide prepared by hydrothermal

N. M. Shaalan[1,2] · D. Hamad[2] · Adil Alshoaibi[1] · A. Y. Abdel-Latief[2] · M. A. Abdel-Rahim[2]

Abstract

The quantum size of materials is an effective property for specific physical applications. The theoretical approach helps in understanding the physical properties of these materials. SnO_2 quantum crystals of ~ 1.8–6.0 nm are prepared by a hydrothermal method. The size of crystals is smaller than the Debye length reported for SnO_2 at 250 °C. The emission spectra of the radiative recombination between conduction and valence bands show a blue shift, which confirms the electron confinement. The prepared materials are used for fabricating gas sensor tested for CH_4 gas. The gas detecting measurements exhibited high sensitive quantum crystals, QCs, toward CH_4. For the first time, a theoretical approach is formulated for the response of SnO_2 toward CH_4 to understand the sensing mechanism of the quantum crystals. The correlation between the theoretical and experimental results clarified the reason of the high response observed for the quantum crystals toward CH_4. To conduct a high response, the crystal size should be comparable or less than the Debye length, which means that the crystal is fully depleted or in volume-depleted in the air. Thus, the high response obtained here is explained in terms of the proposed theoritical approach.

1 Introduction

Controlling the growth of the quantum crystals is essential for different applications. Also, the theoretical study of their quantum size is effective for understanding the performance of materials and their operation mechanism, as well. Improvement of the binary oxide nanomaterials to reach a high sensitivity and precise limitation can be achieved by controlling their growth and the thermal stability of these nanomaterials. Up to date, SnO_2 has the attention of the researchers for gas sensing applications [1–4]. In some studies, the sensitivity realized toward the gas by using multi-element composites can be achieved if the material size is well controlled. The sensors fabricated by SnO_2 nanomaterials are promising sensors toward methane gas.

The methane gas is the main reason for the global warming and can replace oxygen and causes suffocation and explosion [5]. For the public health and environmental safety, on-site detection of methane is important. For detecting methane there are several expensive and bulky techniques are employed [6]. They are multifaceted in the operating procedures and not convenient for on-site use. Several research papers studied the oxide materials for methane detection [1–4, 7–18], but most of these materials show a low sensitivity toward methane at high operating temperatures. To our best knowledge, there is no theoretical approach proved the sensing mechanism of methane by oxide materials.

As it is known, the resistivity of an n-type oxide decreases upon exposure to a reducing gas, such as CH_4, due to the reduction of the depletion layer. Thus, the large depletion

✉ N. M. Shaalan
nshaalan@aun.edu.eg; nmohammed@kfu.edu.sa

✉ Adil Alshoaibi
adshoaibi@kfu.edu.sa

D. Hamad
noniatypes@yahoo.com

A. Y. Abdel-Latief
atta552001@yahoo.com

M. A. Abdel-Rahim
maabdelrahim@yahoo.com

1 Physics Department, Faculty of Science, King Faisal University, Al-Hassa, P.O. Box 400, Hofuf 31982, Saudi Arabia

2 Physics Department, Faculty of Science, Assiut University, Assiut 71516, Egypt

layer of n-type materials is very important parameter for the sensing material. In other words, the fully depleted particle in the air is preferred to achieve a high sensitivity. The fully depletion is realized if the crystal size is less than twice the depth of the depletion layer which mainly depends on the adsorbed oxygen and intrinsic electrons in the bulk (defined by Debye length). The depletion layer of a thin film and sintered powders of SnO_2 is about 3.0 nm at 250 °C as achieved by References [19, 20]. Thus, if the size of SnO_2 becomes less than or comparable to ~ 6.0 nm, dramatically change in gas sensing performances toward the reducing gases may be observed.

In the current study, we attempt to synthesize thermally stable quantum crystals of SnO_2 with size less than 6.0 nm to achieve the above mention goal. The synthesis is carried out by a hydrothermal method-modified with cetyltrimethylammonium (CTAB), which acts as a template for SnO_2 during the growth. The crystal structure and thermal stability are studied by XRD and DTA. The confirmation of the confinement effect is optically investigated. CH_4 sensing is systematically studied at various operating temperatures. A theoretical approach based on the reaction of adsorbed oxygen on the surface and the reaction of methane gas with the oxygen species is proposed to explain the obtained experimental results.

2 Experimental details

For the preparation of SnO_2, hydrate tin chloride ($SnCl_4 \cdot 5H_2O$) was dissolved in distilled water, and then NaOH water-dissolved was added drop-wise to the tin solution. An amount of 1.0 g of CTAB was added into the mixture. The mixture was transferred to a Teflon-lined stainless-steel autoclave. The autoclave was maintained at different temperatures of 100, 120, 140, 160, and 180 °C for 10 h. Afterward, the product was centrifuged for obtaining the powder, which was washed with distilled water and ethanol and then dried at 60 °C/1 h.

The crystalline phase was examined by X-ray diffractometer (model; Philips PW 1700, Cu-Kα) in range 15° to 90° with a speed of 0.06°/s. Scanning electron microscope (SEM) and high-resolution transmission electron microscope (HRTEM) (JEOL-JEM-2100 F) are used for the morphology and crystallinity confirmation. Fluorescence (FL) spectra were recorded in range 300 to 480 nm at room temperature by using Spectrofluorometer (Jasco, FP-6300 WRE) with an excitation wavelength of 290 nm. The fine powder was used to study the thermal behavior using thermal analysis techniques TGA and DTA [SHIMADZU DTA-60H] simultaneous apparatus in the air atmosphere under non-isothermal condition. A constant weight of 5.0 mg was used to drop off the effect of sample weight on the peak

shape and temperature. Non-isothermal DTA thermo-grams were obtained at selected heating rates of 5–25 K/min in the temperature range of 30 up to 800 °C.

The tested gas sensor was fabricated by coating a layer of the fine powder on two gold electrodes deposited by DC sputtering. The fabricated sensor was thermally annealed at 400 °C for 30 min in the ambient air before inserting it into the testing chamber. The operating temperature was varied from the room temperature up to 400 °C. Dry synthetic air mixed with various CH_4 concentrations flows with 200 ml/min rate to the testing chamber, which was connected to Horiba mass flow controllers (SEC-N112 MGM) for flow rate control, and computerized data acquisition (LXI Agilent 34972 A) for electrical measurements.

3 Results and discussions

3.1 Quantum confinement and thermal stability

XRD pattern of SnO_2 rutile tetragonal structure is shown in Fig. 1. The broadening of the diffraction peaks is an indicator for the growth of the fine crystals. The crystallinity of SnO_2 was enhanced by raising the hydrothermal temperature from 100 up to 180 °C. For the samples prepared at 160 and 180 °C, new diffraction peaks with less broadening are observed, showing more crystal orientations and higher crystallinity compared to the others. The powder of SnO_2 was annealed at 400 °C for 2 h. After annealing, the increase in crystallite size is insignificant, which confirms the thermal stability of the as-prepared product.
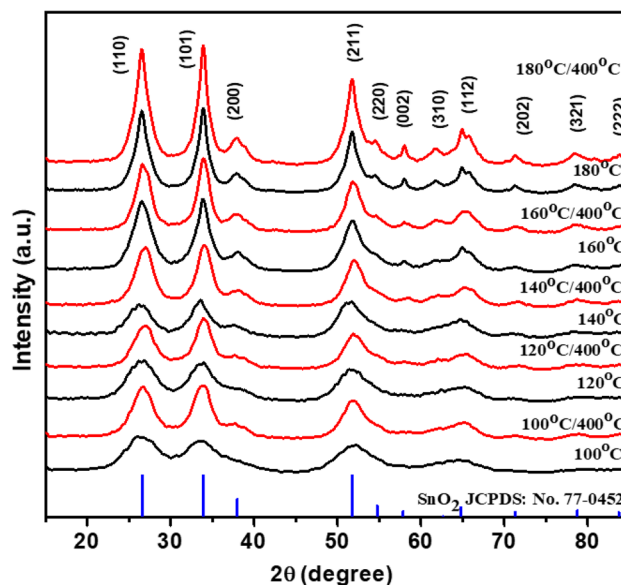

Fig. 1 XRD patterns of SnO_2 quantum crystals before and after the annealing at 400 °C for 2 h

The morphology of annealed SnO_2 is shown in Fig. 2. Directional growth of grass-like structure based on quantum crystals, QCs, is observed after annealing for the samples prepared in 100–140 °C. The growth of grass-like structure has the same crystallite size as indicated in HRTEM shown in Fig. 3. The crystal size was distributed in a range of 1.75–4.25 nm, and 2.5–7.5 nm corresponding to an average size of ~2.5 and 5.0 nm for the preparation temperatures of 120 and 180 °C, respectively. The average size insignificant increased from 2.5 up to 3.6 nm and from 5.0 up to 5.8 nm after the annealing, as shown in Fig. 4.

The optical properties are used for confirming the confinement property of the fine materials. Thus, FL spectra were reported here in the wavelength range of 310–350 nm with an excitation wavelength of ($\lambda_{ex}=290$ nm). The normalized emission spectra of as-prepared and annealed SnO_2 are shown in Fig. 5a and b. The FL spectra exhibited a blue shift with reducing the SnO_2 size. The emission peaks can be attributed to the band edge emission that was caused due to the radiative recombination. As well known, if the size of nanocrystals is comparable or smaller than the quantum size, a stronger confinement exists, and the carriers become confined in this size [21].

The thermal behavior of SnO_2 was simultaneously studied at different heating rates of 5 K/min up to 25 K/min. A typical example of a combined plot of TGA/DTA for the SnO_2 prepared at 120 °C at a heating rate of 15 K/min is shown in Fig. 6a. The first region (I) which extends from 30 to 150 °C with a weight loss about 7% corresponds to an endothermic peak in DTA thermo-gram is due to the elimination of the physically adsorbed water on the surface of SnO_2. The second region (II) which extends from 200 to 400 °C with a weight loss of 5%, corresponding to an exothermic peak in DTA thermo-gram may be due to the elimination of a little amount of the chemically bonded water in SnO_2 molecules. The third region (III) which extends after 400 °C with no weight loss reveals the thermal stability of SnO_2 in this temperature range. A typical example of the TGA/DTA thermo-grams shown in Fig. 6b for SnO_2 prepared at 120 °C after annealing at 400 °C/2 h reveals the absence of the exothermic peak. It means that the grown SnO_2 crystals are thermally stable. On the other hand, the XRD patterns for the annealed samples prepared at 100, 120, and 140 °C reveal the decrease of peak broadening and an increase of the peak intensity compared to
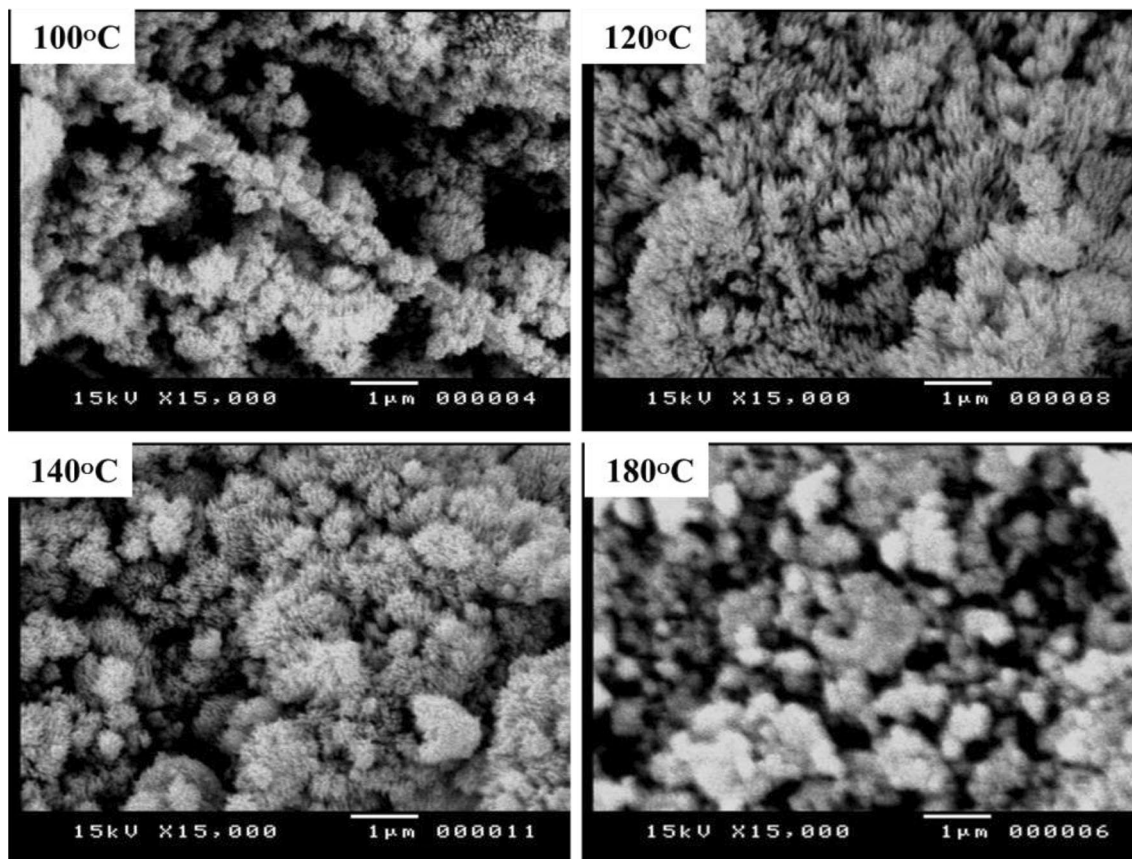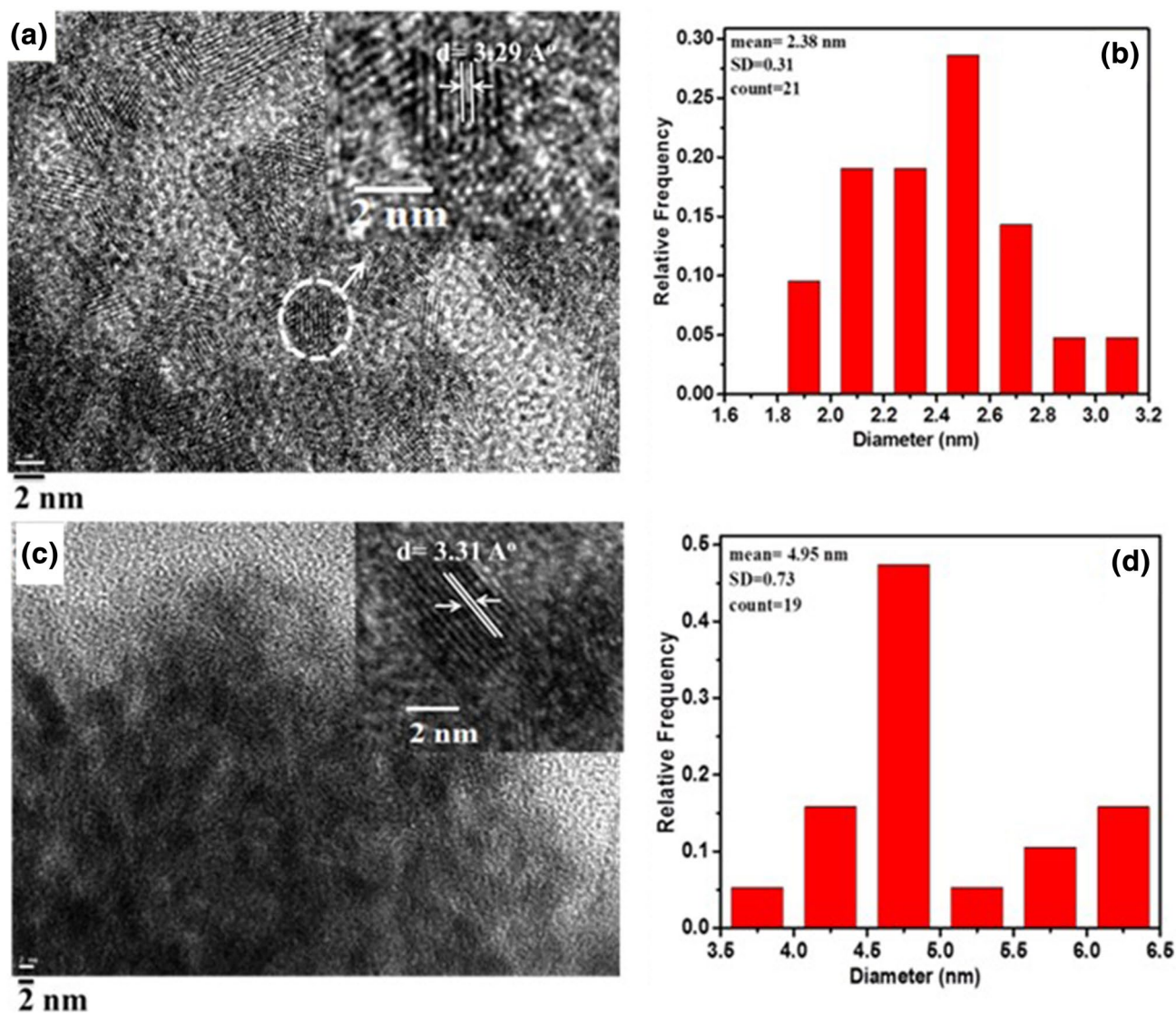

Fig. 2 SEM images of SnO_2 observed after annealing of SnO_2 prepared at 100–180 °C

118   Journal of Materials Science: Materials in Electronics (2020) 31:115–124

Fig. 3 Typical HRTEM images of as-prepared SnO₂ QCs; **a** 120, **c** 180 °C, **b**, and **d** the corresponding crystallite size distribution histograms

the as-prepared samples. This indicates a small increase in both the crystallite size (*D*) with annealing.

3.2 Sensing toward CH₄ gas

The as-prepared SnO₂ is insensitive and its signal is not stable even at high temperatures, as shown in Fig. 7. Furthermore, the existence of gas causes an increase in the sensor resistance which is irregular behavior of reducing gas with n-type materials. This may be attributed to the change observed in the DTA curve in the range of 200–400 °C. The chemically bonded water molecules may prevent adsorbed oxygen to react with the surface or causes a barrier between oxygen and conduction electrons. The elimination of water molecules causes that the sensor is unstable, as well. Thus, we have considered the heat treatment for SnO₂ at

400 °C/2 h. Consequently, the sensor response has been dramatically improved, as shown in Fig. 8. The decrease in resistance due to the exposure to CH₄ gas confirms the n-type behavior of SnO₂. SnO₂ conductance is reduced in the air due to the chemisorption of oxygen, however, the chemisorbed oxygen ions react with CH₄ and increasing the electrical conductance due to the injection of the captured electrons into the conduction band of the oxide.

The dependence of the response on the crystallite size as a function of operating temperature is shown in Fig. 9. The sensor prepared with very fine crystals is the most sensitive toward CH₄. It is clearly seen that the sensor response improved largely with increasing the reciprocal size (1/*D*) larger than 0.22/nm (less than 4.54 nm). It is expected that this size is fully depleted or volume-depleted in the air. These sensors show shorter response
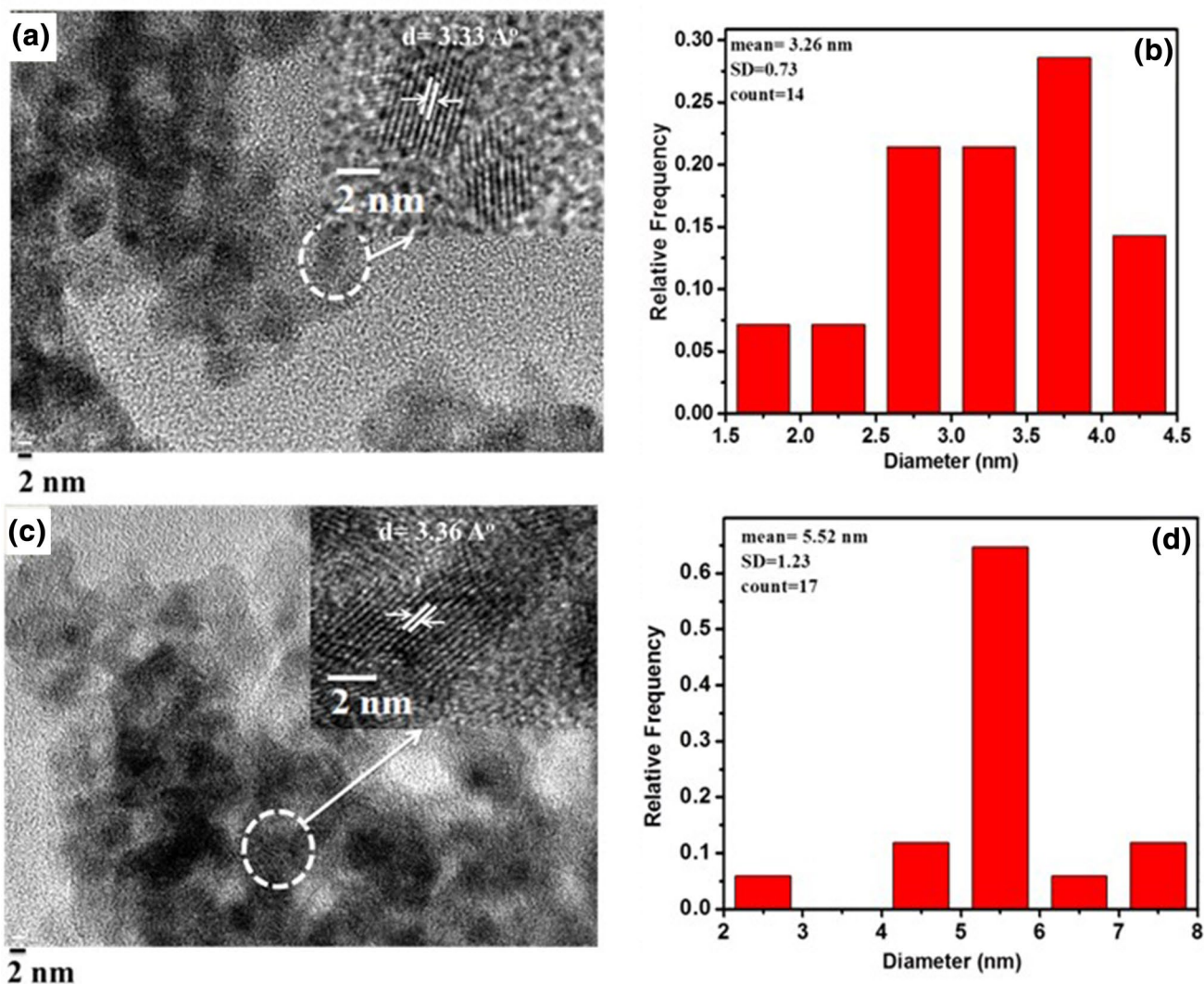
Fig. 4 Typical HRTEM images of SnO$_2$ QCs after annealing at 400 °C/2 h prepared at temperature, **a** 120, **c** 180 °C, **b**, and **d** the corresponding crystallite size distribution histograms

and recovery times compared with those prepared with larger crystals. The short response and recovery times are attributed to the nanograss-like structure formed by a combination of the fine crystals. It is thought that the gas diffusion and adsorption/desorption process throughout this structure are faster. The sensor response toward CH$_4$ of the present SnO$_2$ QCs is much better than the reported in some literature, as listed in Table 1. The results are well interpreted if a theoretical approach based on a real condition is developed. Thus, we have proposed a theoretical calculation based on the reaction of CH$_4$ with the oxygen species.

3.3 Theoretical response of SnO$_2$ toward methane

Methane (denoted B) reacts with oxygen ions on the surface of crystal semiconductor followed the two reactions.

$$O_2 + 2e = 2O^- > 200°C \quad \text{(in air)}, \tag{1}$$

and then

$$B + 2O^- \rightarrow product + 2e \quad \text{(in gas)} \tag{2}$$
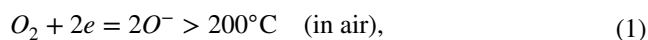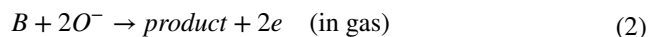
The reaction (1) indicates the capture of electrons by oxygen molecules in the air, forming a depletion layer, as shown in Fig. 10. Reaction (2) is the reverse process, which injects the electrons back into the conduction band of the oxide. The chemical equilibrium of adsorbed oxygen on the oxide surface is expressed by:

$$\left(K_{O_2}P_{O_2}\right)[e]_s^2 = [O^-]^2 \tag{3}$$

where P_{O_2} is the partial pressure of oxygen, K_{O_2} the adsorption constant, $[e]_s$ the density of conduction electrons, and
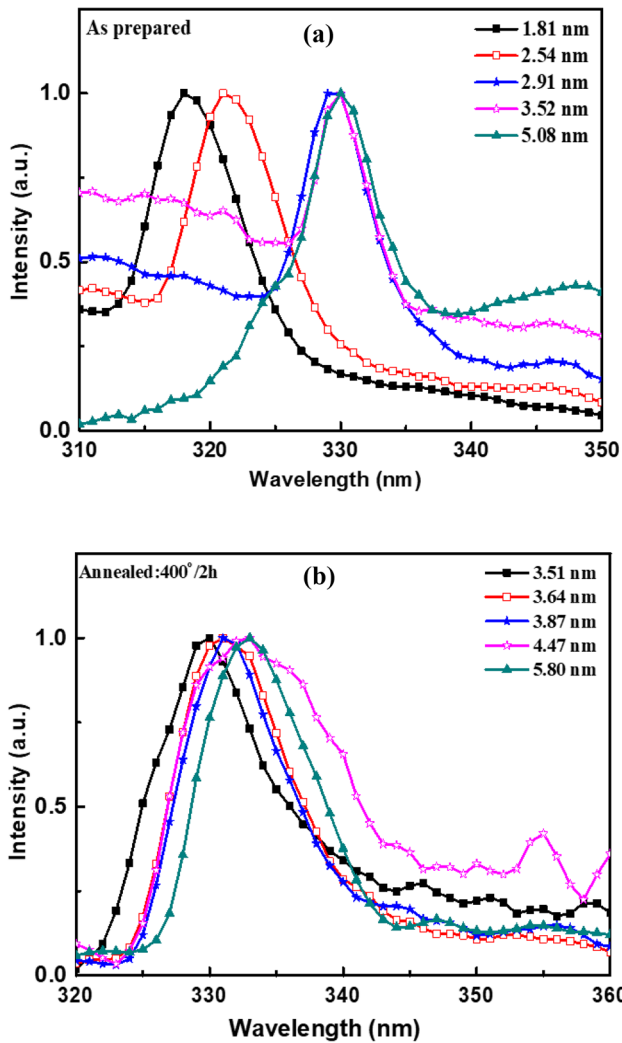
Fig. 5 FL emission spectra at an excitation wavelength of 290 nm; **a** as-prepared and **b** annealed SnO$_2$

Fig. 6 TGA/DTA curves at a heating rate (15 K/min) for the as-prepared and annealed SnO$_2$

$[O^-]$ the surface charge density of oxygen ions. The reduced adsorptive of oxygen is defined by $X = \left(K_{O_2}P_{O_2}\right)^{1/2}/L_D$, here L_D is Debye length defined as $L_D = \left(q^2 N_d/\epsilon k T\right)^{-1/2}$, where N_d is the donor density, ϵ the permittivity material, q the elementary charge, k the Boltzmann constant, and T the absolute temperature.

The adsorption/desorption rate of $[O^-]$ and CH$_4$ is applying as a steady state process. Thus, the above two reactions in equilibrium are expressed as:

$$k_1\left(P_{O_2}\right)[e]_s^2 = k_{-1}[O^-]^2 + k_3 P_{CH4}[O^-]^2 \tag{4}$$

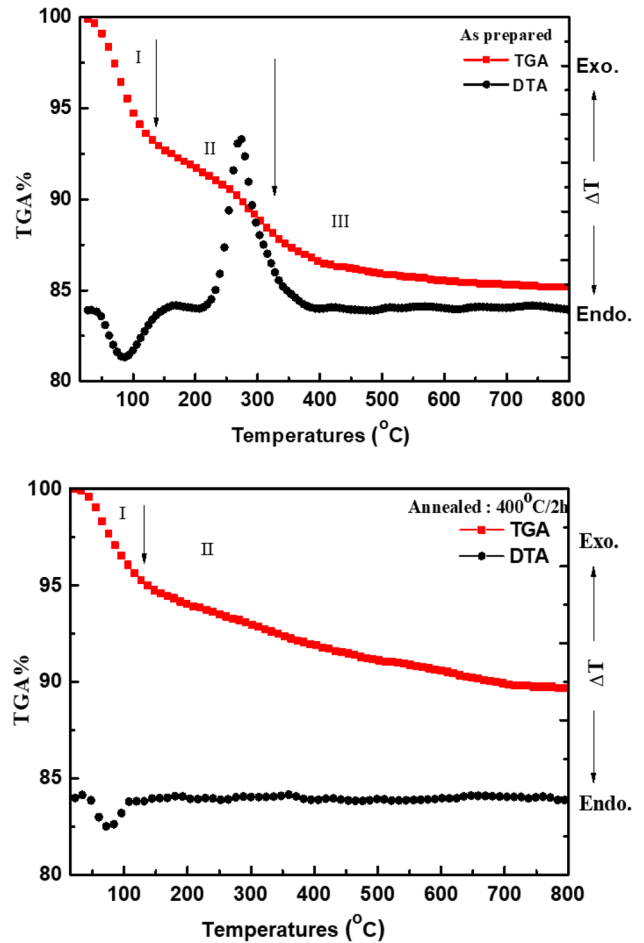$$\frac{k_1}{k_{-1}}\left(P_{O_2}\right)[e]_s^2 = [O^-]^2\left[1 + \frac{k_3}{k_{-1}}P_{CH4}\right] \tag{5}$$
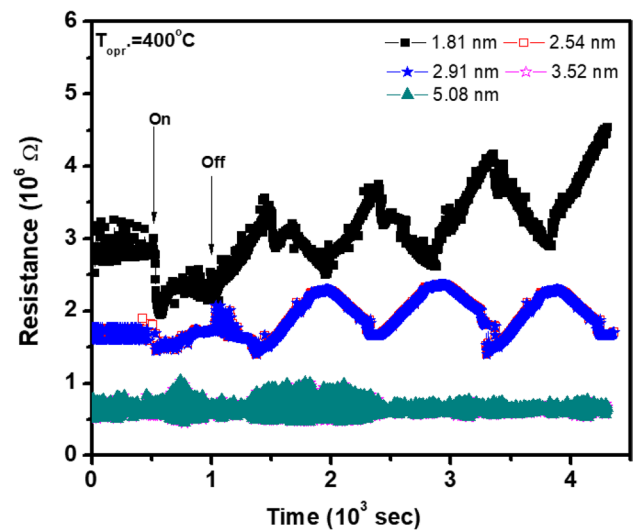

Fig. 7 Sensor signal for as-prepared SnO$_2$ at an operating temperature of 400 °C
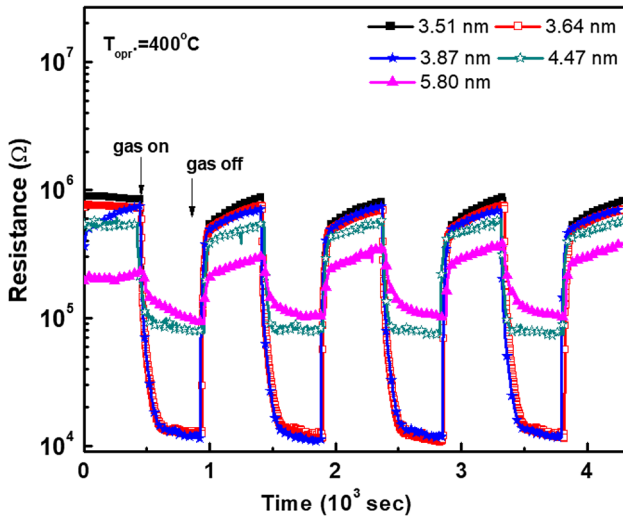
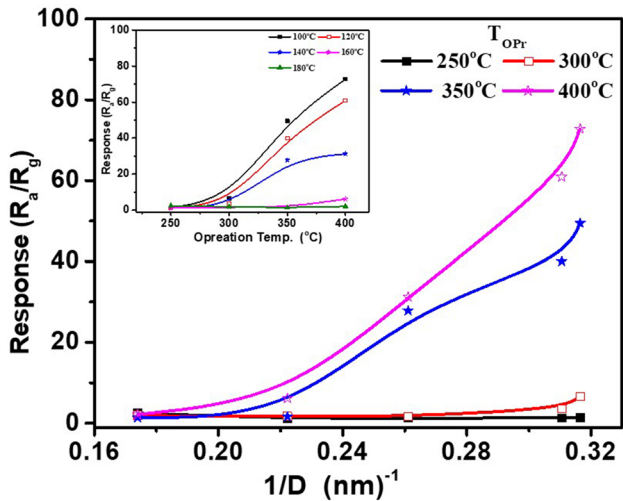**Fig. 8** Sensor signal of annealed SnO_2 at the operating temperature of 400 °C

Table 1 Comparison sensing characteristic of this work with other recent studies

Sensing material	Operating temp. (°C)	$CH_4\%$	Response R_g/R_a	References
Porous 3D SnO_2	120	0.05	1.8	[1]
SnO_2 NR–NP-Gr hybrids	150	1.00	50	[2]
Pt/SnO_2	400	0.50	30	[3]
$PdPt-SnO_2$-rGO	150	69.5	0.1	[4]
Co_3O_4 NPs	200	1.00	1.28	[10]
$Pt-SnO_2$	350	0.10	4.50	[11]
$Ag–SnO_2$	430	0.20	1.75	[12]
SnO_2	250	0.1	20.0	[13]
SnO_2@rGO, PANI	27	1.0	1.9	[14]
$Sn_{0.9-x}In_{0.1}Cu_xO_2$	400	0.25	9.00	[15]
$Pd-SnO_2$	400	0.66	20.0	[16]
SnO_2 Qs	350	1	49.44	Present
	400		72.76	

Fig. 9 Sensor response versus the reduced size of SnO_2 nanostructures and operating temperature

$$X^2[e]_s^2 = [O^-]^2[1 + Y] \qquad (6)$$

Here, Y is the partial pressure of the reducing gas (CH_4). k_1 and k_{-1} are the rate constants of forward reaction in Eq. (1) and the reverse reaction in Eq. (2), respectively. In the absence of B ($P_{CH_4} = 0$), the Eq. (4) coincides with Eq. (3). The density of conduction electrons and the surface charge density of oxygen ions O^- are defined as [22, 23]:

$$[e]_s = N_d \exp\left\{-\frac{qV_r}{kT}\right\}, \text{ and} \qquad (7)$$

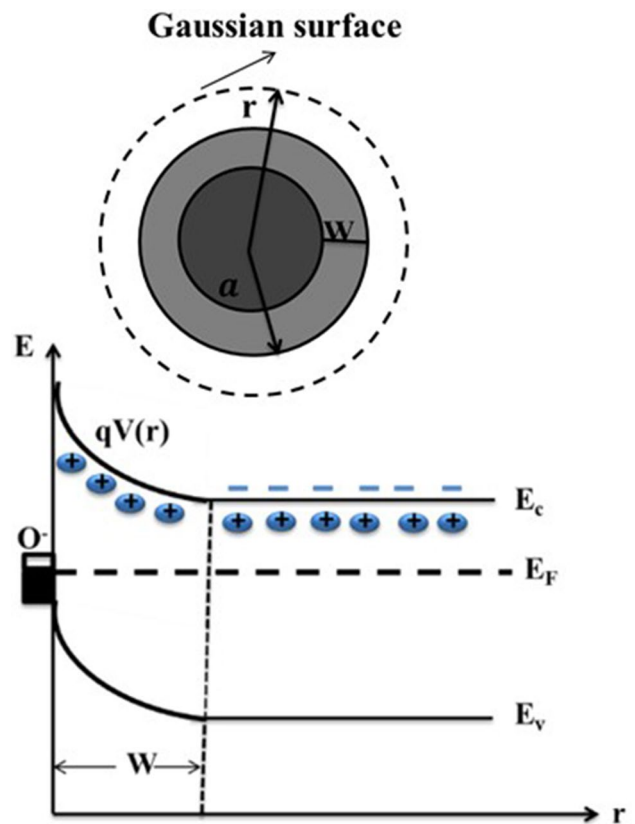$$[O]^- = N_d L_D \left[\frac{n}{3} - \frac{(n-m)^3}{n^2} - A_c\right] \qquad (8)$$

Fig. 10 Formation of the depletion layer for n-type oxide under exposure to an oxygen atmosphere

where n, m, and A_c are the reduced radius of the SnO_2 sphere, reduced depletion layer and correction term considering the electrons left behind in the depleted region, respectively.

Based on Fig. 10, the potential energy for the sphere crystals in the air is given by the following equation: and,

$$\frac{qV_r}{kT} = \left(\frac{1}{3}\right)\left[\frac{n^2}{2} - \frac{3}{2}(n-m)^2 + \frac{(n-m)^3}{n}\right] \quad \text{(regional depletion)}$$

(9)

and

$$\frac{qV_v}{kT} = \frac{qV_b}{kT} + p = \left[\frac{n^2}{6} + p\right] \quad \text{(volume depletion)}$$

(10)

Under the presence of CH_4, the correlation between the depletion layer and gas concentration is determined based on the dependence of the depletion layer formed in the air:

$$X = \left\{\frac{n}{3}\left(1 - \left(\frac{n-m_a}{n}\right)^3\right) - A_c\right\}$$
$$\times \exp\left\{\frac{m_a^2}{6}\left(1 + \frac{2(n-m_a)}{n}\right)\right\} \quad \text{(regional depletion)}$$

(11)

$$then \; X_v = \left\{\frac{n}{3} - A_c \exp(-p_a)\right\}\exp\left\{\frac{n^2}{6} + p_a\right\} \quad \text{(volume depletion)}$$

(12)

where m_a and P_a stand for the depletion layer and the extending in Fermi level in the presence of air. The volume depletion is the dominant mechanism ($m = n$ and Fermi level shift by $pk_B T$) in case of sphere radius is less than the double of Debye length.

To the precise calculation of the sphere response, the conductance is calculated based on the change in the depth of the depletion layer (m). Thus, the sphere is assumed to be partially depleted as shown in Fig. 10, and then the conductance, G is expressed as.

$$G = \int_0^{n-m} \frac{A\sigma_B}{2\pi R}dR(bulk region) + \int_{n-m}^n \frac{A\sigma(R)}{2R}dR(depleted region)$$

(13)

where $\sigma_B = q\mu_B N_d$ and $\sigma(R) = q\mu_B[e]_s$ are the conductivities of bulk, and depleted region, respectively. $R = r/L_D$, is the reduced sphere radius. Thus, the conductance is expressed as:

$$G = c \int_0^{n-m} RdR + c \int_{n-m}^n R\exp\left\{-\frac{qV_r}{kT}\right\}dR \quad \text{(Regional depletion)}$$

(14)

$$G = c \int_0^n R\exp\left\{-\frac{qV_v}{kT}\right\}dR \quad \text{(Volume depletion)}$$

(15)

Thus, the sensor responses, SR, toward CH_4 is calculated using Eqs. (6)–(13) as:

$$SR = \frac{G_g}{G_a}$$

(16)

where G_a and G_g are the conductance of the sensor in the air and in CH_4, respectively. Thus, we consider Eq. (14)
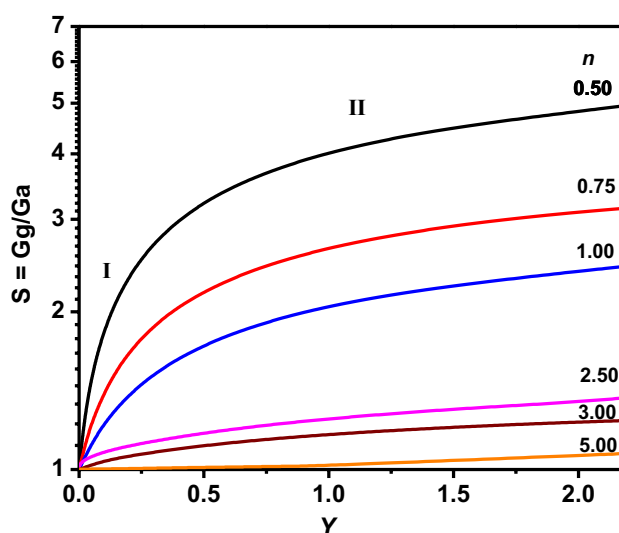

Fig. 11 Calculated response versus CH_4 gas concentration for the variously reduced radius of the SnO_2 sphere. Note: In the region, I, the increase in sensor response is proportional to the gas concentration, but it is insignificant in region II. This explains the importance of fully depleted particles

for the calculation of SR if the crystal is large and partially depleted. While Eq. (15) is considered for the fine crystal which is fully depleted in air. Upon the exposure CH_4, the crystal may be transferred from a volume to regional depletion, thus, both Eqs. (14) and (15) are used. Based on these theoretical bases, the calculated sensitivity as a function of CH_4 concentration is shown in Fig. 11. The crystals which were in a volume depletion in the air are highly sensitive than those in a regional depletion. The sensor response tends to a steady value with more increase in the gas concentration. The steady values are dependent on the radius of the sphere, where it raises up with decreasing the radius. It may be logic to say that the depletion layer formed due to oxygen ions in the air is bit-by-bit reduced with increasing CH_4 concentration. Therefore, the higher gas concentration had a negligible effect on the electrical conductivity, resulting in a less change in the sensor response with a further increase in the gas concentration. Figure 12 shows the calculated response as a function of the reduced radius at gas concentrations of 0.5, 1.0, and 2.0. The response of the large sphere ($1/n < 0.375$) which is partially depleted in the air is very low, because of the depletion layer thickness compared to bulk crystals is small. Moreover, the electron transfer can take place through the bulk area far from the surface. The response was much improved with the fine sphere ($1/n > 0.375$) which was in a volume depletion in the air.

A similar result is drawn for the experimental part shown in Fig. 9. This result suggests that the QCs with 3.5 nm and 3.6 nm in the presence of air are fully depleted, while the
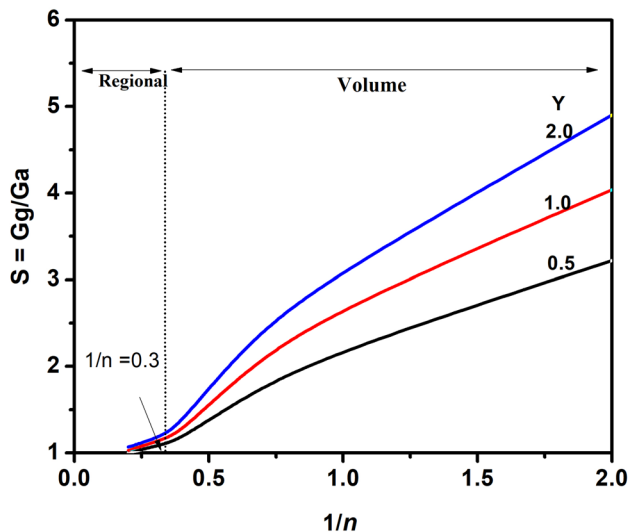
Fig. 12 Calculated response versus the reciprocal radius of the sphere. Note: the sensor response is very low in regional depletion ($1/n < 0.3$ or $n > 3.3$), but it is high in volume depletion or $n < 3.3$

larger QCs are partially depleted in the same condition. It is a reasonable result where the Debye length of SnO_2 in the air is about ~ 3.0 nm at 250 °C, suggesting that the crystals with 6.0 nm might be regional-depleted, and 3.0 nm is volume depleted in the air. The current proposed approach is appropriate for the interpretation of the reaction mechanism of the methane gas with the n-type oxide.

4 Conclusions

Thermal stable SnO_2 quantum crystals with a size smaller than the Debye length were synthesized. The thermal annealing has an insignificant effect on the crystallite size but has a significant effect on the gas sensing properties. The QCs grew in nanograss-like structure with a directional growth of (110). This structure with its small crystals showed a high response and short response and recovery times toward methane. The crystal size of the prepared SnO_2 is comparable or smaller than the Debye length of SnO_2, which allowed for the QCs to be a fully depleted or volume-depleted in the air. Consequently, the gas has a large chance to react with much oxygen species and has a significant impact on oxide conductivity. A theoretical approach is proposed for explaining the gas sensing mechanism of CH_4 and SnO_2. The proposed theoretical calculation confirmed this expectation and suggested that the fine crystals were volume-depleted in the air, whareas, the larger crystals were regional-depleted. Thus, the fine crystals expressed a high response toward CH_4 gas, while the larger crystals expressed a low response.

References

1. D. Xue, S. Zhang, Z. Zhang, Hydrothermally prepared porous 3D SnO_2 microstructures for methane sensing at lower operating temperature. Mater. Lett. **237**, 336–339 (2019)
2. M. Kootia, S. Keshtkara, M. Askariehb, A. Rashidi, Progress toward a novel methane gas sensor based on SnO_2 nanorods nanoporous graphene hybrid. Sens. Actuators B **281**, 96–106 (2019)
3. F.S. Fateminia, Y. Mortazavi, A.A. Khodadadi, Au-promoted Ce-Zr catalytic filter for Pt/SnO_2 sensor to selectively detect methane and ethanol in the presence of interfering indoor gases. Mater. Sci. Semicond. Process. **90**, 182–189 (2019)
4. S. Navazani, A. Shokuhfar, M. Hassanisadi, A.D. Carlo, N.Y. Nia, A. Agresti, A PdPt decorated SnO_2-rGO nanohybrid for high-performance resistive sensing of ethane. J. Taiwan Inst. Chem. Eng. **95**, 438–451 (2019)
5. S. Nasresfahani, M.H. Sheikhi, A. Tohidi, A. Zarifkar, Methane gas sensing properties of Pd-doped SnO_2/reduced graphene oxide synthesized by a facile hydrothermal route. Mater. Res. Bull. **89**, 161–169 (2017)
6. X. Liu, S. Cheng, H. Liu, S. Hu, D. Zhang, H. Ning, A survey on gas sensing technology. Sensors **12**, 9635–9665 (2012)
7. A. Das, V. Bonu, A.K. Prasad, D. Panda, S. Dhara, A.K. Tyagi, The role of SnO_2 quantum dots in improved CH_4 sensing at low temperature. J. Mater. Chem. C **2**, 164–171 (2014)
8. G. Fedorenko, L. Oleksenko, N. Maksymovych, G. Skolyar, O. Ripko, Semiconductor Gas Sensors Based on Pd/SnO_2 Nanomaterials for Methane Detection in Air. Nanoscale Res. Lett. **12**, 329–338 (2017)
9. P. Dhivya, A.K. Prasad, M. Sridharan, Effect of sputtering power on the methane sensing properties of nanostructured cadmium oxide films. J. Alloy. Comp. **620**, 109–115 (2015)
10. N.M. Shaalan, M. Rashad, A. Moharram, M. Abdel-Rahim, Promising methane gas sensor synthesized by microwave-assisted Co_3O_4 nanoparticles. Mater. Sci. Semi. Process. **46**, 1–5 (2016)
11. W. Lu, D. Ding, Q. Xue, Y. Du, Y. Xiong, J. Zhang, X. Pan, W. Xing, Great enhancement of CH_4 sensitivity of SnO_2 based nanofibers by heterogeneous sensitization and catalytic effect. Sens. Actuators B **254**, 393–401 (2018)
12. Z.K. Horastani, S.M. Sayedi, M.H. Sheikhi, E. Rahimi, Effect of silver additive on electrical conductivity and methane sensitivity of SnO_2. Mater. Sci. Semi. Process. **35**, 38–44 (2015)
13. S. Navazani, A. Shokuhfar, M. Hassanisadi, M. Askarieh, A.D. Carlo, A. Agresti, Facile synthesis of a SnO_2@rGO nanohybrid and optimization of its methane-sensing parameters. Talanta **181**, 422–430 (2018)
14. S. Navazani, A. Shokuhfar, M. Hassanisadi, A.D. Carlo, N. Shahcheraghi, Fabrication and characterization of a sensitive, room

temperature methane sensor based on SnO_2 @reduced graphene oxide-polyaniline ternary nanohybrid. Mater. Sci. Semicond. Process. **88**, 139–147 (2018)

15. S. Somacescu, P. Osiceanu, J.M. Calderon-Moreno, A. Sackmann, C.E. Simion, A. Stănoiu, Mesoporous $Sn_{0.9-x}In_{0.1}Cu_x(I)O_{2-\delta}$ gas sensors with selectivity to H_2S working under humid air conditions. Micro. Meso. Mater. **197**, 63–71 (2014)

16. T. Wagner, M. Bauer, T. Sauerwald, C.D. Kohl, M. Tiemann, X-ray absorption near-edge spectroscopy investigation of the oxidation state of Pd species in nanoporous SnO_2 gas sensors for methane detection. Thin Solid Films **520**, 909–912 (2011)

17. S. Basu, P.K. Basu, Nanocrystalline metal oxides for methane sensors: role of noble metals, J. Sens. **2009**, 861968 (2009)

18. W. Chen, Q. Zhou, L. Xu, F. Wan, S. Peng, W. Zeng, Improved methane sensing properties of co-doped SnO2 electrospun nanofibers. J. Nanomater. **2013**, 4 (2013)

19. C. Xu et al., Relationship between gas sensitivity and microstructure of porous SnO_2. J. Electrochem. Soc. Jpn. **58**, 1143–1148 (1990)

20. H. Ogawa, M. Nishikawa, A. Abe, Hall measurement studies and an electrical conductive model of tin oxide ultrafine particle films. J. Appl. Phys. **53**, 4448–4454 (1982)

21. W. Wei, H. Xu, Q. You, Q. Cheng, C. Liu, L. Zou, X. Liu, Preparation of quantum dot luminescent materials through the ink approach. Mater. Des. **91**, 165–170 (2016)

22. N. Yamazoe, K. Suematsu, K. Shimanoe, Extension of receptor function theory to include two types of adsorbed oxygen for oxide semiconductor gas sensors. Sens. Actuators B **163**, 128–135 (2012)

23. N. Yamazoe, K. Shimanoe, Theoretical approach to the rate of response of semiconductor gas sensor. Sens. Actuators B **150**, 132–140 (2010)